Applied Physics Letters

Giant magnetoelectric effect in an $L2_1$-ordered $Co_2FeSi/Pb(Mg_{1/3}Nb_{2/3})O_3$-$PbTiO_3$ multiferroic heterostructure

Cite as: Appl. Phys. Lett. **118**, 142402 (2021); https://doi.org/10.1063/5.0044094
Submitted: 14 January 2021 • Accepted: 21 March 2021 • Published Online: 06 April 2021

T. Usami, S. Fujii, S. Yamada, et al.

AIP Publishing

Applied Physics Letters ARTICLE scitation.org/journal/apl

Giant magnetoelectric effect in an $L2_1$-ordered $Co_2FeSi/Pb(Mg_{1/3}Nb_{2/3})O_3$-$PbTiO_3$ multiferroic heterostructure

Cite as: Appl. Phys. Lett. **118**, 142402 (2021); doi: 10.1063/5.0044094
Submitted: 14 January 2021 · Accepted: 21 March 2021 ·
Published Online: 6 April 2021

View Online Export Citation CrossMark

T. Usami,[1,a)] S. Fujii,[2] S. Yamada,[1,2] Y. Shiratsuchi,[1,3] R. Nakatani,[1,3] and K. Hamaya[1,2,a)]

AFFILIATIONS

[1]Center for Spintronics Research Network, Graduate School of Engineering Science, Osaka University, Toyonaka, Osaka 560-8531, Japan
[2]Department of Systems Innovation, Graduate School of Engineering Science, Osaka University, Toyonaka, Osaka 560-8531, Japan
[3]Division of Materials and Manufacturing Science, Graduate School of Engineering, Osaka University, Suita, Osaka 565-0871, Japan

[a)]**Authors to whom correspondence should be addressed:** usami@ee.es.osaka-u.ac.jp and hamaya@ee.es.osaka-u.ac.jp

ABSTRACT

We experimentally show a giant magnetoelectric (ME) effect at room temperature in an interfacial multiferroic heterostructure consisting of $L2_1$-ordered Co_2FeSi and $Pb(Mg_{1/3}Nb_{2/3})O_3$-$PbTiO_3$ (PMN-PT). Molecular beam epitaxy growth at 400 °C enables us to obtain epitaxial and $L2_1$-ordered Co_2FeSi films on PMN-PT(001). For the epitaxial Co_2FeSi/PMN-PT heterostructure, the remanent magnetization state can be largely modulated by varying electric fields. We note that the room-temperature ME coupling coefficient (α) is estimated to be 6.0–6.3 $\times 10^{-6}$ s/m, comparable to the highest α value reported previously. Nonvolatile and repeatable magnetization changes in remanent states are also demonstrated. These results will pave the way for room-temperature electric-field control of the magnetization of half-metallic Heusler alloys in high-performance spintronic devices.

As a next-generation memory for semiconductor integrated circuits with low power consumption, the magnetoresistive random access memory (MRAM) has been studied because of its high-speed, repeatable, and nonvolatile operation.[1–3] In general, writing data through the magnetization switching processes by applying electric currents consumes a large electric power in spin-transfer torque or spin–orbit torque MRAMs. To tackle the problem in these MRAMs, the magnetization switching induced by applying electric fields has been proposed, in which less power consumption is expected.[4]

To date, the electric field magnetization manipulation has been achieved in several special systems such as multiferroic insulator oxides,[5,6] ferromagnetic (FM) semiconductors,[7,8] and ultra-thin FM atomic layers.[9,10] In addition to these systems, artificial FM/ferroelectric (FE) multiferroic heterostructures have recently been explored because of potential advantages for room-temperature operation and a wide variety of material selections.[11–14] For the electric field magnetization manipulation in FM/FE multiferroic heterostructures, several mechanisms via magnetostriction, exchange bias, charge accumulation, and redox have been proposed.[11] Among these mechanisms, the magnetostriction effect is particularly important to effectively modulate the magnetization states in the FM layer through the piezostrains induced in the FE layer. Also, the magnetostriction from the FE layer is a long-range scale effect and induces a relatively large modulation of the magnetization state in the FM layer.[11,12]

For these reasons, an FE material, $Pb(Mg_{1/3}Nb_{2/3})O_3$-$PbTiO_3$ (PMN-PT), having a large piezoelectric constant ($d_{33} \sim 2000$ pm/V),[15,16] has been explored, where a schematic for the crystal structure of PMN-PT is illustrated in Fig. 1(a). Actually, PMN-PT has been widely studied in FM/FE multiferroic heterostructures with a combination of many FM materials: $(La,Sr)MnO_3$,[17,18] Fe_3O_4,[19] FeGa,[20] CoFeB,[21,22] and common ferromagnetic materials such as Fe,[23] Co,[24,25] Ni,[26] and their alloys.[27–29] Among a variety of FM materials, Co-based Heusler alloys have attracted interest from the viewpoint of MRAM applications because they have high spin polarization leading a high magnetoresistance ratio in tunnel magnetoresistance junctions.[30–33] However, only the experimental study of a Co_2FeAl (CFA)/PMN-PT multiferroic heterostructure has been reported because of

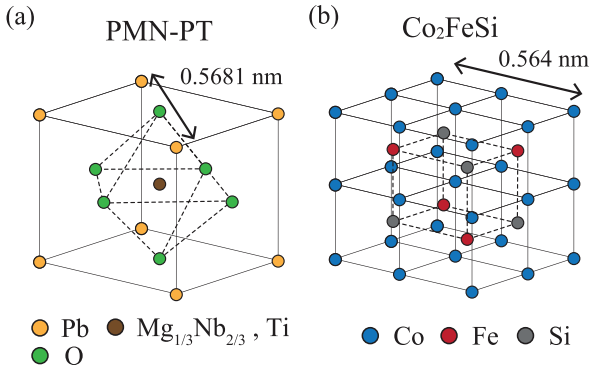

FIG. 1. Schematic crystal structures of (a) $Pb(Mg_{1/3}Nb_{2/3})O_3$-$PbTiO_3$ and (b) Co_2FeSi.

the growth difficulty.[34,35] In fact, although the formation of the $L2_1$-ordered structure is required for the high-performance operation, it is limited that the reported CFA/PMN-PT was composed of $B2$-ordered or polycrystalline CFA films. As a result, the large magnetoelectric (ME) effect in the CFA/PMN-PT heterostructure at room temperature has not been reported yet.

Here, we concentrate on Co_2FeSi (CFS), which has been expected to be a half metal with a high Curie temperature of 1100 K.[36] A schematic for the crystal structure of CFS is shown in Fig. 1(b). Notably, we have shown that the epitaxial and $L2_1$-ordered CFS films can be experimentally grown on oxides[37,38] or semiconductor structures.[39–41] In this Letter, we experimentally demonstrate an epitaxial and $L2_1$-ordered CFS/PMN-PT(001) multiferroic heterostructure using a molecular beam epitaxy (MBE) technique at 400 °C. For the epitaxial Co_2FeSi/PMN-PT heterostructure, the remanent magnetization state can be largely modulated by varying electric fields. The room-temperature ME coupling coefficient (α) is estimated to be $(6.3\pm0.2)\times10^{-6}$ s/m, comparable to the highest α value reported previously.[22] In addition, nonvolatile and repeatable magnetization changes in remanent states are demonstrated. These results will pave the way for room-temperature electric-field control of the magnetization of half-metallic Heusler alloys in high-performance spintronic devices.

First, we explain the crystal structures of PMN-PT and CFS, shown in Figs. 1(a) and 1(b), respectively. PMN-PT has a perovskite structure, it can be considered as a pseudocubic, and the lattice constant of PMN-PT is 0.4017 nm with the 30% PT composition,[16] while CFS is a cubic and an $L2_1$ ordered structure with a lattice constant of 0.564 nm.[42] Thus, the mismatch between the diagonal length of the lattice constant of PMN-PT and the lattice constant of CFS is approximately 0.7%. As a result, the epitaxial growth of CFS films on PMN-PT(001) can be expected.

For the CFS/PMN-PT heterostructure, we next explain the growth procedure of CFS films on PMN-PT(001). 30-nm-thick CFS thin films were grown on single-crystal PMN-PT(001) substrates at 200 or 400 °C by MBE. Prior to the growth, the heat treatment was performed at 600 °C for 15 min to obtain a flat surface of PMN-PT(001). After cooling down to the growth temperature of 200 or 400 °C, the CFS film was grown by co-evaporating using Knudsen cells, where we set the supplied atomic composition ratio of Co:Fe:Si to 2.0:1.0:1.0 during the growth.[37,39] After the growth, *in situ* reflection high-energy electron diffraction (RHEED) images are observed, as shown in Figs. 2(a) and 2(b). For the CFS film grown at 400 °C, symmetrical streak patterns are observed in the RHEED image [Fig. 2(a)], indicating two-dimensional epitaxial growth. In contrast, the CFS film grown at 200 °C shows the ring-like RHEED patterns [Fig. 2(b)], indicating the formation of polycrystalline films. θ-2θ x-ray diffraction (XRD) patterns for the CFS films grown at 400 and 200 °C are shown in Figs. 2(c) and 2(d), respectively. Only for the CFS film grown at 400 °C, evident 004 and 002 diffraction peaks are observed, indicating that the film is (001)-oriented epilayers. The out-of-plane lattice constant of the CFS film grown at 400 °C is 0.563 nm, slightly smaller than the bulk value of 0.564 nm.[42] Here, energy dispersive x-ray spectroscopy (EDX) measurements reveal that the grown CFS film has a slightly Co-rich composition (Co:Fe:Si = 2.27:0.91:0.82). We infer that the slight difference in the lattice constant between the grown film and bulk is due to the compositional deviation and/or the in-plane tensile strain from the PMN-PT(001) substrate. From these results, we can form the two-different CFS/PMN-PT heterostructures (epitaxial or polycrystalline) by varying the growth temperatures.

Figure 3(a) shows the {111} diffraction peaks of the 400 °C-grown CFS film (top) and the used PMN-PT(001) substrate (bottom) in XRD ϕ-scan measurements. The fourfold {111} peaks in the top of Fig. 3(a) indicate the presence of the $L2_1$ structures in the 400 °C-grown CFS film. By a comparison of the {111} peaks between the CFS film and PMN-PT(001), we conclude the epitaxial relationship, CFS[100](001)‖PMN-PT[110](001) as shown in Fig. 3(b). Using the results in such XRD measurements, we estimate the degree of $B2$ and $L2_1$ order parameters, S_{B2} and S_{L2_1}, respectively, only for the 400 °C-grown CFS film. The values of S_{B2} and S_{L2_1} are expressed as follows:[43,44]

$$S_{B2}=\sqrt{\frac{I_{002}/I_{004}}{I^R_{002}/I^R_{004}}},\quad S_{L2_1}=\frac{2}{3-S_{B2}}\sqrt{\frac{I_{111}/I_{202}}{I^R_{111}/I^R_{202}}},\tag{1}$$

where I_{hkl} and I^R_{hkl} are the experimental and theoretical diffraction peak intensities for the hkl plane. As a result, the values of S_{B2} and S_{L2_1}

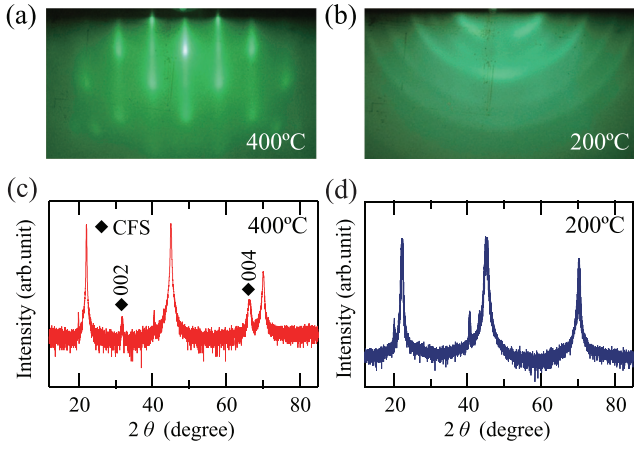

FIG. 2. RHEED images for the Co_2FeSi films grown at (a) 400 °C and (b) 200 °C with the incident electron beam along the PMN-PT[110] direction. XRD profiles in θ-2θ scan for Co_2FeSi films grown at (c) 400 °C and (d) 200 °C.

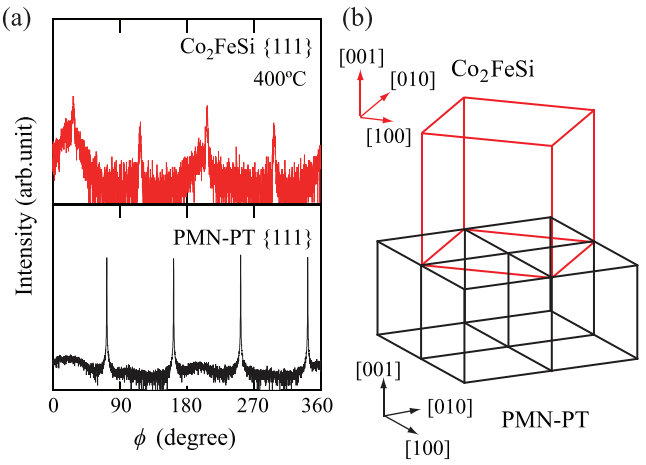

FIG. 3. (a) XRD ϕ-scan profiles for {111} of the Co_2FeSi film grown at 400 °C (top) and the PMN-PT(001) substrate (bottom). (b) Schematic illustration of the epitaxial relationship between the Co_2FeSi film grown at 400 °C and the PMN-PT(001) substrate. The red and black arrows denote the crystallographic orientations for the Co_2FeSi film and the PMN-PT substrate, respectively.

are estimated to be 0.94 and 0.80, respectively. According to EDX measurements, since it was revealed that there is a slight deviation of the atomic compositions in CFS films, we should consider the presence of the structural disorder as a reason for S_{B2}, $S_{L2_1} < 1.0$ even in the epitaxial CFS/PMN-PT(001) heterostructure. However, we can regard $L2_1$-ordered structures as the dominant phase in the present CFS/PMN-PT(001) heterostructure.

Magnetic properties of the CFS/PMN-PT(001) heterostructures are examined using a vibrating sample magnetometer (VSM) at room temperature (27 °C). Figure 4 shows in-plane magnetization curves for the CFS/PMN-PT(001) heterostructures formed at 400 °C (epitaxial) and at 200 °C (polycrystalline), where the direction of the applied external magnetic field (H) is along PMN-PT[100]. For the epitaxial CFS/PMN-PT(001) heterostructures, the saturation magnetization

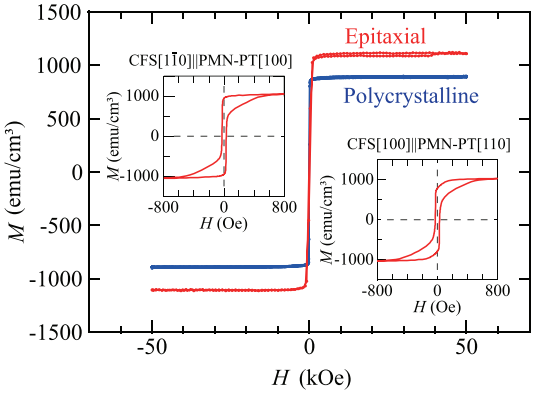

FIG. 4. Magnetization curves of the epitaxial (red) and polycrystalline (blue) Co_2FeSi films. The external magnetic field is applied along the PMN-PT[100] direction. The insets show expanded views of the magnetization curves of the epitaxial film under the magnetic fields along $Co_2FeSi[1\bar{1}0]$ || PMN-PT[100] and Co_2FeSi[100] || PMN-PT[110]. All the measurements were performed at 27 °C.

(M_S) is estimated to be 1110 ± 40 emu/cm^3 (5.4 ± 0.2 μ_B/f.u.), close to M_S for the CFS epilayers with a high spin polarization of 0.7–0.8.[45] On the other hand, the value of M_S for the polycrystalline CFS/PMN-PT(001) heterostructure is 890 ± 30 emu/cm^3 (4.3 ± 0.1 μ_B/f.u.), relatively low compared to that for the epitaxial CFS/PMN-PT(001) heterostructure. We infer that the above difference in M_S is derived from the difference in the crystal quality because there is almost no sharp diffraction peak in Fig. 2(d).[46] The insets of Fig. 4 show the enlarged magnetization curves for the epitaxial CFS/PMN-PT(001) heterostructure, measured under the magnetic fields along CFS[1$\bar{1}$0] || PMN-PT[100] (left) and CFS[100] || PMN-PT[110] (right). The magnetization reversal behavior of the epitaxial CFS/PMN-PT(001) heterostructure is slightly changed by applying the different magnetic-field directions. In contrast, the polycrystalline CFS/PMN-PT(001) heterostructure showed an isotropic feature (not shown here). From these structural and magnetic characterization studies, we regard the epitaxial CFS/PMN-PT(001) heterostructure as a high-quality FM/FE multiferroic system.

To characterize the electric-field effect on magnetic properties for the CFS/PMN-PT(001) heterostructures, we perform magneto-optical Kerr effect measurements at room temperature with and without applying electric fields (E). Here, Au(100 nm)/Ti(3 nm) backside electrodes are deposited on the bottom of the PMN-PT(001) substrate, which enables us to apply E to the CFS/PMN-PT(001) heterostructures along the PMN-PT[001] direction. Figure 5(a) shows room-temperature hysteresis loops of the Kerr rotation angle (θ_K) for the epitaxial (top) and polycrystalline (bottom) CFS/PMN-PT(001) heterostructures by applying E, where H is applied along the in-plane [100] direction of the PMN-PT substrate. Notably, we can clearly see that the value of the saturation Kerr-rotation angle (θ_K^{sat}) for the epitaxial CFS/PMN-PT(001) heterostructure is larger than that for the polycrystalline CFS one. In addition, the shape of the Kerr hysteresis loop for the epitaxial CFS/PMN-PT(001) heterostructure is markedly modulated by changing E from +8.0 to −8.0 kV/cm, while the shape of the Kerr loops is slightly varied by changing E for the polycrystalline CFS/PMN-PT(001) heterostructure.

To explore the electric field modulation in detail, we also measure the remanent Kerr rotation (θ_K^{rem}) vs E for both the CFS/PMN-PT(001) heterostructures, as shown in Fig. 5(b). For the measurement, we first apply an E value of −8 kV/cm and vary the amplitude of E from −8.0 to +8.0 kV/cm and then back to E = −8.0 kV/cm. The sweep rate of E is 20 V/cm/s. For the epitaxial CFS/PMN-PT(001) heterostructure, θ_K^{rem} sharply increases or decreases at $E \sim \pm 1$ kV/cm upon increasing or decreasing E from −8.0 kV/cm or +8.0 kV/cm, respectively. We find that the value of E showing the abrupt change in θ_K^{rem} is close to a reported coercive field of PMN-PT(001).[47] Also, the E dependence shows a hysteretic behavior, implying the nonvolatile variation in remanent magnetization states. In general, there are two types of piezoelectric polarization vector switchings along ⟨111⟩ in the pseudocubic unit cell of PMN-PT,[16,21,47] in which one is the 109° polarization switching and the other is the 71/180° one. The former causes an in-plane strain variation rotated by 90° along ⟨110⟩ in PMN-PT(001) although the latter dose not induce the rotation of the strain.[21,47] Thus, for an application of E to PMN-PT[001], a hysteric feature seen in Fig. 5(b) is related to the 109° switching inducing the in-plane-strain rotation. In addition to this, since the value of θ_K^{sat} for the epitaxial CFS/PMN-PT(001) heterostructure is nearly constant for all the Kerr

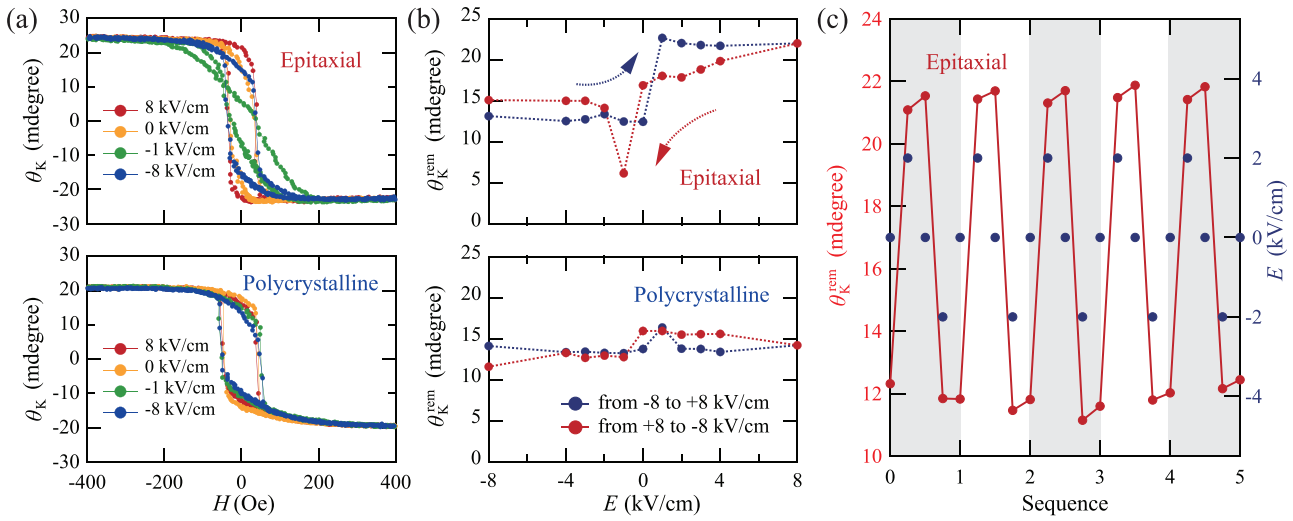

FIG. 5. (a) Magneto-optical Kerr loops for the epitaxial (top) and polycrystalline (bottom) CFS/PMN-PT(001) heterostructures at various E values at room temperature. The external magnetic field (H) is applied along the PMN-PT[100] direction. (b) E dependence of the remanent Kerr rotation θ_K^{rem} for the epitaxial (top) and polycrystalline (bottom) CFS/PMN-PT(001) heterostructures at room temperature. (c) Demonstration of the switching of the remanent Kerr rotation (red) for the epitaxial CFS/PMN-PT(001) heterostructure at room temperature. The magnitude of E is applied with the bipolar sequence (blue).

hysteresis loops in Fig. 5(a), we can conclude that the E-field-dependent θ_K^{rem} originates from the modulation of the in-plane magnetic anisotropy induced by the in-plane-strain variation, as reported in many FM/PMN-PT systems.[21,35,48,49] Contrary to this, the polycrystalline CFS/PMN-PT(001) heterostructure does not show such a large variation in θ_K^{rem} with increasing and decreasing E. Taking into account these facts, we can regard the large E effect on the remanent magnetization (M_{rem}) as a consequence of the piezoelectric induced strain change at the epitaxial CFS/PMN-PT(001) interface.

To quantitatively evaluate the ME effect for the CFS/PMN-PT(001) heterostructures, we define the ME coefficient α as follows:

$$\alpha = \mu_0 \frac{dM}{dE} = \mu_0 \frac{M_{rem}(E) - M_{rem}(E=0)}{E}, \quad (2)$$

where μ_0 is the vacuum permeability. Here, we define dM as the difference in the remanent magnetizations between before and after the application of E, where this method has been established in previous studies of FM/FE systems.[21,22,50] Note that dM in Eq. (2) is different from that for conventional ME substances such as Cr_2O_3 for which dM is defined as the induction of spontaneous magnetization by E.[51] To indirectly deduce M_{rem}, we assume that the value of θ_K^{sat} ($\sim$23.9 $\pm$ 0.1 mdeg) corresponds to the value of M_S (1110 $\pm$ 40 emu/cm^3) measured by VSM. On the basis of the above assumption, M_{rem} is estimated as $M_{rem} = M_S \times (\theta_K^{rem}/\theta_K^{sat})$. As a result, the α values of $(6.0\pm0.2) \times 10^{-6}$ s/m and $(6.3\pm0.2) \times 10^{-6}$ s/m are obtained at E changing from 0 to +1 kV/cm and at E changing from 0 to -1 kV/cm, respectively, for the epitaxial CFS/PMN-PT(001) heterostructure. On the other hand, the polycrystalline CFS/PMN-PT(001) heterostructure gives smaller α values of 1.5–1.9 $\times 10^{-6}$ s/m at the same E value. Notably, the α values estimated here mean the magnitude of the strain-mediated ME effect at the formed CFS/PMN-PT heterointerfaces. Compared to the previous reports in such systems, the present values of α for the epitaxial CFS/PMN-PT(001) heterostructure are comparable to those of amorphous CoFeB/PMN-PT(011) (8×10^{-6} s/m)[22] and CoFeB/PMN-PT(001) (2×10^{-6} s/m),[21] the highest α value in reported FM/FE interfacial multiferroic systems. In the case of the previous amorphous CoFeB,[22] the α value increased upon changing the PMN-PT crystal orientations from (001) to (011) where the largest change in the piezostrain was expected.[29] If we can form the epitaxial CFS/PMN-PT(011) heterostructure, further enhancement in the α value can be expected.

Finally, repeatable switchings of the remanent magnetization states with nonvolatile nature are shown in Fig. 5(c), where the sequence of the E application to PMN-PT[001] is also displayed in the right vertical axis. Evident variations in two magnetic states with high/low θ_K^{rem} can be repeatably demonstrated at room temperature. Because the magnetization vector switching does not need an application of H, the repeatable and nonvolatile magnetization control at the remanent states can be utilized as a part of the technology for voltage-induced magnetization switching in storage and/or memory devices with high-quality Co-based Heusler alloys.[33,52–54]

In summary, we demonstrated an epitaxial and $L2_1$-ordered $Co_2FeSi/Pb(Mg_{1/3}Nb_{2/3})O_3$-$PbTiO_3$ multiferroic heterostructure with giant α values of 6.0–6.3 $\times 10^{-6}$ s/m. Nonvolatile and repeatable magnetization changes in remanent states were also achieved, meaning the utilization for a part of the technology for voltage-induced magnetization switching in storage and/or memory devices with high-performance Co-based Heusler alloys.

The authors appreciate Professor Tomoyasu Taniyama of Nagoya University for fruitful discussions. This work was partly supported by JST CREST, Grant No. JPMJCR18J1.

DATA AVAILABILITY

The data that support the findings of this study are available from the corresponding author upon reasonable request.

REFERENCES

[1]A. D. Kent and D. C. Worledge, Nat. Nanotechnol. **10**, 187 (2015).
[2]S. Bhatti, R. Sbiaa, A. Hirohata, H. Ohno, S. Fukami, and S. Piramanayagam, Mater. Today **20**, 530 (2017).
[3]S. Yuasa and D. D. Djayaprawira, J. Phys. D: Appl. Phys. **40**, R337 (2007).
[4]J.-M. Hu, Z. Li, L.-Q. Chen, and C.-W. Nan, Nat. Commun. **2**, 553 (2011).
[5]H. Schmid, Ferroelectrics **162**, 317 (1994).
[6]N. A. Spaldin and R. Ramesh, Nat. Mater. **18**, 203 (2019).
[7]H. Ohno, D. Chiba, F. Matsukura, T. Omiya, E. Abe, T. Dietl, Y. Ohno, and K. Ohtani, Nature **408**, 944 (2000).
[8]F. Matsukura, Y. Tokura, and H. Ohno, Nat. Nanotechnol. **10**, 209 (2015).
[9]T. Maruyama, Y. Shiota, T. Nozaki, K. Ohta, N. Toda, M. Mizuguchi, A. A. Tulapurkar, T. Shinjo, M. Shiraishi, S. Mizukami, Y. Ando, and Y. Suzuki, Nat. Nanotechnol. **4**, 158 (2009).
[10]B. Dieny and M. Chshiev, Rev. Mod. Phys. **89**, 025008 (2017).
[11]J.-M. Hu and C.-W. Nan, APL Mater. **7**, 080905 (2019).
[12]J.-M. Hu, C.-G. Duan, C.-W. Nan, and L.-Q. Chen, npj Comput. Mater. **3**, 18 (2017).
[13]T. Taniyama, J. Phys. Condens. Matter **27**, 504001 (2015).
[14]C. A. F. Vaz, J. Phys. Condens. Matter **24**, 333201 (2012).
[15]Y. Guo, H. Luo, D. Ling, H. Xu, T. He, and Z. Yin, J. Phys. Condens. Matter **15**, L77 (2003).
[16]B. Noheda, D. E. Cox, G. Shirane, J. Gao, and Z.-G. Ye, Phys. Rev. B **66**, 054104 (2002).
[17]S. P. Pati and T. Taniyama, J. Phys. D: Appl. Phys. **53**, 054003 (2020).
[18]C. Thiele, K. Dörr, S. Fähler, L. Schultz, D. C. Meyer, A. A. Levin, and P. Paufler, Appl. Phys. Lett. **87**, 262502 (2005).
[19]M. Liu, J. Hoffman, J. Wang, J. Zhang, B. Nelson-Cheeseman, and A. Bhattacharya, Sci. Rep. **3**, 1876 (2013).
[20]W. Jahjah, J.-P. Jay, Y. L. Grand, A. Fessant, A. Prinsloo, C. Sheppard, D. Dekadjevi, and D. Spenato, Phys. Rev. Appl. **13**, 034015 (2020).
[21]S. Zhang, Y. G. Zhao, P. S. Li, J. J. Yang, S. Rizwan, J. X. Zhang, J. Seidel, T. L. Qu, Y. J. Yang, Z. L. Luo, Q. He, T. Zou, Q. P. Chen, J. W. Wang, L. F. Yang, Y. Sun, Y. Z. Wu, X. Xiao, X. F. Jin, J. Huang, C. Gao, X. F. Han, and R. Ramesh, Phys. Rev. Lett. **108**, 137203 (2012).
[22]J. Wang, D. Pesquera, R. Mansell, S. van Dijken, R. P. Cowburn, M. Ghidini, and N. D. Mathur, Appl. Phys. Lett. **114**, 092401 (2019).
[23]C. Zhang, F. Wang, C. Dong, C. Gao, C. Jia, C. Jiang, and D. Xue, Nanoscale **7**, 4187 (2015).
[24]W. Zhou, C. Ma, Z. Gan, Z. Zhang, X. Wang, W. Tan, and D. Wang, Appl. Phys. Lett. **111**, 052401 (2017).
[25]C. Zhou, C. Zhang, J. Yao, and C. Jiang, Appl. Phys. Lett. **109**, 112404 (2016).
[26]T. Wu, A. Bur, P. Zhao, K. P. Mohanchandra, K. Wong, K. L. Wang, C. S. Lynch, and G. P. Carman, Appl. Phys. Lett. **98**, 012504 (2011).
[27]X. Han, L. Xi, Y. Li, X. Guo, D. Li, Z. Wang, Y. Zuo, and D. Xue, Appl. Phys. Lett. **105**, 122402 (2014).
[28]M. Liu, W. Du, H. Su, B. Liu, H. Meng, and X. Tang, Appl. Phys. Lett. **116**, 152401 (2020).
[29]W. Du, M. Liu, H. Su, H. Zhang, B. Liu, H. Meng, G. Xu, R. Peng, and X. Tang, Appl. Phys. Lett. **117**, 222401 (2020).
[30]S. Trudel, O. Gaier, J. Hamrle, and B. Hillebrands, J. Phys. D: Appl. Phys. **43**, 193001 (2010).
[31]Y. Sakuraba, M. Hattori, M. Oogane, Y. Ando, H. Kato, A. Sakuma, T. Miyazaki, and H. Kubota, Appl. Phys. Lett. **88**, 192508 (2006).
[32]W. Wang, H. Sukegawa, R. Shan, S. Mitani, and K. Inomata, Appl. Phys. Lett. **95**, 182502 (2009).
[33]Z. Wen, H. Sukegawa, S. Mitani, and K. Inomata, Appl. Phys. Lett. **98**, 192505 (2011).
[34]G. Dunzhu, F. Liu, Y. Wang, C. Zhou, and C. Jiang, Mater. Res. Express **6**, 066114 (2019).
[35]C. Zhou, G. Dunzhu, J. Yao, and C. Jiang, J. Alloys Compd. **710**, 680 (2017).
[36]S. Wurmehl, G. H. Fecher, H. C. Kandpal, V. Ksenofontov, C. Felser, H.-J. Lin, and J. Morais, Phys. Rev. B **72**, 184434 (2005).
[37]K. Kudo, Y. Hamazaki, S. Yamada, S. Abo, Y. Gohda, and K. Hamaya, ACS Appl. Electron. Mater. **1**, 2371 (2019).
[38]S. Yamada, Y. Teramoto, D. Matsumi, D. Kepaptsoglou, I. Azaceta, T. Murata, K. Kudo, V. K. Lazarov, T. Taniyama, and K. Hamaya, Phys. Rev. Mater. **5**, 014412 (2021).
[39]S. Yamada, K. Hamaya, K. Yamamoto, T. Murakami, K. Mibu, and M. Miyao, Appl. Phys. Lett. **96**, 082511 (2010).
[40]K. Kasahara, K. Yamamoto, S. Yamada, T. Murakami, K. Hamaya, K. Mibu, and M. Miyao, J. Appl. Phys. **107**, 09B105 (2010).
[41]K. Kasahara, Y. Fujita, S. Yamada, K. Sawano, M. Miyao, and K. Hamaya, Appl. Phys. Express **7**, 033002 (2014).
[42]B. Balke, G. H. Fecher, H. C. Kandpal, C. Felser, K. Kobayashi, E. Ikenaga, J.-J. Kim, and S. Ueda, Phys. Rev. B **74**, 104405 (2006).
[43]Y. Takamura, R. Nakane, and S. Sugahara, J. Appl. Phys. **105**, 07B109 (2009).
[44]Y. Takamura, T. Suzuki, Y. Fujino, and S. Nakagawa, J. Appl. Phys. **115**, 17C732 (2014).
[45]K. Hamaya, N. Hashimoto, S. Oki, S. Yamada, M. Miyao, and T. Kimura, Phys. Rev. B **85**, 100404(R) (2012).
[46]Z. Gercsi and K. Hono, J. Phys. Condens. Matter **19**, 326216 (2007).
[47]L. Yang, Y. Zhao, S. Zhang, P. Li, Y. Gao, Y. Yang, H. Huang, P. Miao, Y. Liu, A. Chen, C. W. Nan, and C. Gao, Sci. Rep. **4**, 4591 (2014).
[48]J. J. Yang, Y. G. Zhao, H. F. Tian, L. B. Luo, H. Y. Zhang, Y. J. He, and H. S. Luo, Appl. Phys. Lett. **94**, 212504 (2009).
[49]S. Zhang, Q. Chen, Y. Liu, A. Chen, L. Yang, P. Li, Z. S. Ming, Y. Yu, W. Sun, X. Zhang, Y. Zhao, Y. Sun, and Y. Zhao, ACS Appl. Mater. Interfaces **9**, 20637 (2017).
[50]Y. Wei, C. Gao, Z. Chen, S. Xi, W. Shao, P. Zhang, G. Chen, and J. Li, Sci. Rep. **6**, 30002 (2016).
[51]M. Fiebig, J. Phys. D: Appl. Phys. **38**, R123 (2005).
[52]T. M. Nakatani, T. Furubayashi, S. Kasai, H. Sukegawa, Y. K. Takahashi, S. Mitani, and K. Hono, Appl. Phys. Lett. **96**, 212501 (2010).
[53]S. Li, Y. Sakuraba, T. Sasaki, J. Chen, S. Bosu, and K. Hono, AIP Adv. **8**, 075230 (2018).
[54]M. S. Gabor, T. Petrisor, M. Nasui, M. A. Nsibi, J. Nath, and I. M. Miron, Phys. Rev. Appl. **13**, 054039 (2020).